Influence of dielectrical heating on convective flow in a radial force field

Vadim Travnikov, Florian Zaussinger ⬤, Peter Haun ⬤, and Christoph Egbers

Department of Aerodynamics and Fluid Mechanics, Brandenburg University of Technology Cottbus-Senftenberg,
Siemens-Halske-Ring 14, 03046, Cottbus, Germany

We present results of numerical and experimental investigations of thermal convection induced by internal heating in both a nonrotating and a rotating spherical gap filled with dielectric fluid. The inner and outer surfaces are maintained at constant temperatures T_{in} and T_{out}, respectively. A radial force field is produced due to the dielectrophoretic effect. The buoyancy force in the Navier-Stokes equation and the source term in the energy equation depend on the imposed oscillating electric field according to $V_{\text{rms}}^2 r^{-5}$ and $V_{\text{rms}}^2 r^{-4}$, respectively, where V_{rms} is the root mean squared value of the voltage between spherical surfaces and r is the radial distance. Beginning with the nonrotating case, we perform linear instability analysis in the case of purely internal heating, i.e., both surfaces are maintained at the same temperature $\Delta T = T_{\text{in}} - T_{\text{out}} = 0$. Next, we consider a situation in which there is not only internal heating but also a temperature difference $\Delta T > 0$. While the spherical gap rotated, the occurring two-dimensional steady basic flow was calculated numerically. The stability of the basic flow was investigated by means of linear instability theory. The critical Rayleigh numbers and the critical azimuthal wave numbers are presented in dependence on the Taylor number. We calculate supercritical three-dimensional flows for comparison with experimentally obtained patterns in frames of the GeoFlow experiment on the International Space Station.

I. INTRODUCTION

Because of the geophysical relevance the exploration of the convective flows in the spherical gap was the subject of intensive theoretical and numerical studies. If the inner surface is warmer than the outer one and a fluid is influenced by a central force, then the situation occurs that can be compared with the Rayleigh-Bénard convection. The flow patterns occurring in such simplified configuration have been investigated by Busse and his coworkers in both nonrotating and rotating cases. Whereas the flow patterns in the rotating case are defined by the Coriolis force and the critical azimuthal wave numbers m_c can be derived due to the linear instability theory [1,2], we have completely other situation in the nonrotating case because of the symmetry of the problem under consideration. Patterns of the supercritical flow [3–5] and bifurcation scenarios [6] have been formulated in terms of parameter ℓ (degree of corresponding Legendre polynomial) in this case. The next important motivation for the implementation of the numerical analysis of the convective flows under the influence of the radial force field is the world-wide recognized GeoFlow experiment [7] that takes place on the International Space Station (ISS). The most important advantage of this experiment is that the influence of the Earth's gravity can be eliminated. Hence, if the fluid is heated from within and we find the possibility to produce the central force field, then the Rayleigh-Bénard convection in the spherical geometry can be realized under the microgravity conditions. To produce the radial force field the electric field is imposed on a dielectrical incompressible fluid of density ρ and permittivity $\epsilon(T)$, where T is the temperature. The force density, generated by electric field **E** can be expressed as follows [8]:

$$\mathbf{f}_e = \rho_e \mathbf{E} - \frac{1}{2}\mathbf{E}^2 \nabla \epsilon(T) + \nabla \left[\frac{1}{2} \rho \left(\frac{\partial \epsilon}{\partial \rho} \right)_T \mathbf{E}^2 \right], \quad (1)$$

where the first term is the density of the Coulomb force with a free charge ρ_e. The second term represents the dielectrophoretic force density, $\mathbf{f}_{\text{dep}}$. The third term, corresponding to the electrostriction force, can be combined with the pressure gradient. The Coulomb force is negligible if the frequency of the imposed electric field f is much higher than all frequencies that are responsible for the fluid behavior, e.g., the inverse of the charge relaxation time $\tau_e = \epsilon_0 \epsilon_r / \sigma_e$ (ϵ_0 is the vacuum permittivity, ϵ_r is the dielectric constant σ_e is the electrical conductivity), the inverse of the viscous relaxation time $t_v = d^2/\nu$, and the inverse of the thermal relaxation time $t_\kappa = d^2/\kappa$, where ν is the kinematic viscosity, κ is the thermal diffusivity, and $d = R_2 - R_1$ is the width of the spherical gap. The next condition that must be satisfied to neglect the Coulomb force is $d \gg \delta_D$, where δ_D is the thickness of the Debye layer on the electrodes [9,10]. Because all these conditions fulfilled only the dielectrophoretic force influences the flow and must be taken into account.

The behavior of the electric permittivity can be approximated by a linear function of the temperature T:

$$\epsilon(T) = \epsilon_0 \epsilon_r [1 - \gamma(T - T_{\text{out}})]. \quad (2)$$

The force $\mathbf{f}_{\text{dep}}$ can be written after a little algebra as follows:

$$\mathbf{f}_{\text{dep}} = -\gamma(T - T_{\text{out}})\mathbf{g}_e, \quad \mathbf{g}_e = \frac{\epsilon_0 \epsilon_r}{2\rho} \nabla \mathbf{E}^2, \quad (3)$$

where $\mathbf{g}_e$ is due to the electric field-induced artificial gravity field, and γ is the coefficient of thermal permittivity. Because the dielectrophoretic force $\mathbf{f}_{\mathrm{dep}}$ and the induced artificial gravity have opposite directions, the problem can be compared with the classical Rayleigh-Bénard (RB) problem, with one important difference. Whereas in RB convection the gravity does not change and the flow is controlled due to the temperature gradient, in our case $\Delta T = T_{\mathrm{in}} - T_{\mathrm{out}}$ is maintained at constant value and the flow is triggered by varying the voltage or artificial gravity. Furthermore, volumetric heating is involved in the energy equation due to the source term according to the relation

$$H_E = \frac{2\pi f \epsilon_0 \epsilon_r h_{\mathrm{diss}}}{\rho C_p} \mathbf{E}^2, \qquad (4)$$

where h_{diss} is the energy dissipation factor, and C_p is a specific heat capacity. Therefore, we have electric-field-dependent (via voltage) gravity $g_e \sim V_{\mathrm{rms}}^2 r^{-5}$ in the Navier-Stokes equation [11] and source $H_E \sim V_{\mathrm{rms}}^2 r^{-4}$ in the energy equation. In other words, the source term and the gravity are coupled parameters ($H_E \sim g_e$).

This situation completely differs from the situation in which source and the gravity are independent. In our case the gravity is a source. Hence, it is necessary to construct control parameters such that only one depends on the voltage. These specific parameters for the problem under consideration are discussed in the next section.

The work presented is a numerical support for the well-known GeoFlow experiment [12–14] on the ISS. Whereas the GeoFlow I experiment was performed with fluid of constant viscosity (silicon oil M5), a fluid with temperature-dependent viscosity (1-nonanol) was used during the GeoFlow II experiment. Although the temperature-sensitive viscosity plays an important role, we found that the influence of the internal heating is much more significant and becomes crucial if the frequency of the imposed electric field increases from $f = 50$ Hz (GeoFlow I) to $f = 10650$ Hz (GeoFlow II). Thus, the source term Eq. (4) must be involved in the energy equation. This paper is a sequel to Ref. [15], where the problem under investigation was solved numerically in framework of the GeoFlow I experiment in which the effect of the internal heating is negligible.

The paper is organized as follows. After the governing equations are formulated in Sec. II, we present the numerical method in Sec. III. The structure of the basic flow for different Rayleigh numbers and Taylor numbers is discussed in Sec. IV. Linear instability analysis is performed in Sec. V. Nonlinear calculations of the supercritical three-dimensional flows, analysis of the heat transfer and bifurcation analysis in the nonrotating and rotating cases are presented in Secs. VI A and VI B, correspondingly. Experimental results are discussed in Sec. VI C.

II. EQUATIONS

We consider an incompressible viscous dielectric fluid in the Boussinesq approximation in the spherical gap. In the common form, the problem under consideration can be described due to the Navier-Stokes equation for the velocity

$$\frac{\partial \mathbf{U}}{\partial t} + (\mathbf{U}\boldsymbol{\nabla})\mathbf{U} = -\boldsymbol{\nabla} p_{\mathrm{eff}} - \gamma(T - T_{\mathrm{out}})\mathbf{g}_e + \nu\boldsymbol{\Delta}\mathbf{U}$$
$$- 2\boldsymbol{\Omega} \times \mathbf{U} - \frac{\rho(T)}{\rho_0}\boldsymbol{\Omega} \times (\boldsymbol{\Omega} \times \mathbf{r}), \quad (5)$$

where $\mathbf{U}$ is the velocity field, t is the time,

$$p_{\mathrm{eff}} = \frac{p}{\rho_0} - \frac{\gamma\epsilon_0\epsilon_r(T - T_{\mathrm{out}})E^2}{2\rho_0} - \frac{1}{2}\left(\frac{\partial\epsilon}{\partial\rho}\right)_T E^2, \quad (6)$$

$\rho_0 = \rho(T_{\mathrm{out}})$, $\boldsymbol{\Omega}$ is the rotation rate, the energy equation for the temperature

$$\frac{\partial T}{\partial t} + (\mathbf{U} \cdot \boldsymbol{\nabla})T = \kappa\nabla^2 T + H_E, \qquad (7)$$

the continuity equation

$$\boldsymbol{\nabla} \cdot \mathbf{U} = 0, \qquad (8)$$

and the Gauss equation

$$\boldsymbol{\nabla} \cdot (\epsilon(T)\boldsymbol{\nabla}\upsilon) = 0, \qquad (9)$$

where υ is the electric potential: $\mathbf{E} = -\boldsymbol{\nabla}\upsilon$. Whereas no-slip boundary conditions for the velocity field are used in the study presented, we consider two kinds of boundary conditions for the temperature. If both surfaces are maintained at the same temperature $T_{\mathrm{in}} = T_{\mathrm{out}} = T_b$, then only the internal heating due to the source H_E is responsible for the heat transfer. The situation changes if the inner surface is maintained at a higher temperature than the outer one $T_{\mathrm{in}} > T_{\mathrm{out}}$. In this case the heat transfer is produced not only because of internal heating but also due to conduction. The boundary conditions for the velocity, the temperature and electric potential are

$$\mathbf{U} = 0, \quad T = T_{in}, \quad \upsilon = V_{\mathrm{rms}} \qquad (10)$$

on the inner surface $r = R_1$,

$$\mathbf{U} = 0, \quad T = T_{\mathrm{out}}, \quad \upsilon = 0. \qquad (11)$$

on the outer surface $r = R_2$. Note that real-time-dependent voltage $V(t) = V_0 \cos 2\pi f t$ was replaced by the root mean squared value $V_{\mathrm{rms}} = \sqrt{<V^2(t)>} = V_0/\sqrt{2}$ according to the time-averaged relation over a period of the voltage variation $T_e = f^{-1} <V^2(t)> = \frac{1}{T_e}\int_0^{T_e} V^2(t)dt$. Conditions of this replacement were numerically derived in [16,17] and can be briefly formulated as follows. First, the Prandtl number of the working fluid must be large (Pr $\gg 1$). Furthermore, the frequency f must obey two conditions: $f \gg t_\nu^{-1}$ and $f \gg \tau_e^{-1}$. Taking into account that $f = 10650$ Hz, Pr $= 176$, $\nu = 1.3970 \times 10^{-5}$ m^{2}s^{-1}, $d = R_2 - R_1 = 135$ mm, where R_1 and R_2 are the inner and outer radii, correspondingly, all these conditions are fulfilled (Table I).

Now we have to formulate the governing equations in detail. The first case corresponds to a situation in which only dielectrical heating without rotation ($\Delta T = 0$ K, $\Omega = 0$) is considered. The second one describes not only the effect of dielectrical heating but also a convective effect triggered by the temperature difference between the spherical surfaces and the rotation of the spherical system ($\Delta T > 0$, $\Omega \geqslant 0$). Because we have different boundary conditions for the temperature, it is useful to formulate two sets of equations to

Nomenclature	$T_{\text{out}} = 293$ K
Energy dissipation factor h_{diss}	6.2423×10^{-2}
Volume expansion coefficient $\alpha (\text{K}^{-1})$	8.2343×10^{-4}
Coefficient of thermal permittivity $\gamma (\text{K}^{-1})$	0.010209
AC frequency f(Hz)	1.0650×10^{4}
Permittivity ϵ_r	9.05629
Density ρ (kgm^{-3})	828.16
Specific heat capacity C_p (JK^{-1})	2470
Kinematic viscosity ν (m^{2}s^{-1})	1.3970×10^{-5}
Thermal diffusivity κ (m^{2}s^{-1})	7.94×10^{-8}

be solved. Beginning with the purely dielectrical heating case and writing the equation for $\epsilon(T)$ in the form

$$\epsilon(T) = \epsilon_0 \epsilon_r [1 - \gamma(T - T_b)], \tag{12}$$

We can introduce the dimensionless temperature T^* using $T - T_b = T_b T^*$. Introducing d for the length, κ/d for the velocity and $t_\kappa = d^2/\kappa$ for the time, $\mathbf{E} = \mathbf{E}^* \frac{V_{\text{rms}}}{d}$ for the electric field the Navier-Stokes equation, the energy equation, and the Gauss equation can be written, dropping stars, in the dimensionless form:

$$\text{Pr}^{-1} \left[\frac{\partial \mathbf{U}}{\partial t} + (\mathbf{U} \boldsymbol{\nabla}) \mathbf{U} \right]$$
$$= -\text{Pr}^{-1} \boldsymbol{\nabla} p + \boldsymbol{\Delta} \mathbf{U} - \frac{1}{4} \text{R}_{\text{H}} \cdot T \cdot \boldsymbol{\nabla} [\boldsymbol{\nabla} \upsilon_0(r)$$
$$+ \boldsymbol{\nabla} \upsilon_1 (r, \theta, \phi)]^2, \tag{13}$$

$$\frac{\partial T}{\partial t} + (\mathbf{U} \cdot \boldsymbol{\nabla}) T = \nabla^2 T + \frac{\text{R}_{\text{H}}}{\text{R}_{\text{T}}} [\boldsymbol{\nabla} \upsilon_0(r) + \boldsymbol{\nabla} \upsilon_1 (r, \theta, \phi)]^2, \tag{14}$$

$$\nabla^2 \upsilon_1(r, \theta, \phi) = \frac{\gamma T_b}{1 - \gamma T_b T} \boldsymbol{\nabla} T \cdot [\boldsymbol{\nabla} \upsilon_0(r) + \boldsymbol{\nabla} \upsilon_1 (r, \theta, \phi)], \tag{15}$$

where $\text{R}_{\text{H}} = \frac{2\epsilon_0 \epsilon_r \gamma T_b V_{\text{rms}}^2}{\rho \nu \kappa}$ is the Rayleigh-Roberts number, $\text{R}_{\text{T}} = \frac{C_p \gamma T_b^2}{\pi \nu f h_{\text{diss}}}$. Note that it is useful to divide the electric field $\mathbf{E}$ into two parts (θ is polar angle and ϕ is azimuthal angle)

$$\mathbf{E} = \mathbf{E}_0(r) + \mathbf{E}_1(r, \theta, \phi), \tag{16}$$

$$\mathbf{E}_0(r) = -\boldsymbol{\nabla} \upsilon_0(r), \tag{17}$$

$$\mathbf{E}_1(r, \theta, \phi) = -\boldsymbol{\nabla} \upsilon_1(r, \theta, \phi). \tag{18}$$

Whereas the field $\mathbf{E}_0(r)$, which satisfies an expression $\boldsymbol{\nabla} \cdot \mathbf{E}_0(r) = 0$, can be calculated analytically,

$$\mathbf{E}_0(r) = \frac{\eta}{(1 - \eta)^2} \frac{1}{r^2} \mathbf{e}_r, \tag{19}$$

where $\eta = \frac{R_1}{R_2}$ is a radii ratio, the field $\mathbf{E}_1(r, \theta, \phi)$ has a more complex form because it generally depends on all three coordinates and must be found numerically by solving Eq. (15). The velocity field $\mathbf{U}$, the temperature T, and the electric

potential υ_1 obey

$$\mathbf{U} = 0, \quad T = 0, \quad \upsilon_1 = 0 \tag{20}$$

on the both surfaces $r = \eta/(1 - \eta)$ and $r = 1/(1 - \eta)$.

Substituting $\mathbf{E}_0(r)$ in Eq. (3) we obtain the well-known r^{-5} dependence [11]. It is clear that the second field occurs because of the temperature-dependent function $\epsilon(T)$. In the second case, the equation for the permittivity Eq. (2) and the equation of state

$$\rho(T) = \rho_0 [1 - \alpha(T - T_{\text{out}})] \tag{21}$$

have been substituted in the Navier-Stokes equation. The dimensionless temperature T^* can be expressed in the form $T - T_{\text{out}} = \Delta T T^*$, where $\Delta T = T_{\text{in}} - T_{\text{out}}$. If the same scale is retained for the length, for the velocity, for the time, and for the electric field, then the governing equations can be expressed as follows (omitting stars):

$$\text{Pr}^{-1} \left[\frac{\partial \mathbf{U}}{\partial t} + (\mathbf{U} \boldsymbol{\nabla}) \mathbf{U} \right]$$
$$= -\text{Pr}^{-1} \boldsymbol{\nabla} p + \boldsymbol{\Delta} \mathbf{U} - \frac{1}{4} \text{Ra}_{\text{E}} \cdot T \cdot \boldsymbol{\nabla} [\boldsymbol{\nabla} \upsilon_0(r)$$
$$+ \boldsymbol{\nabla} \upsilon_1 (r, \theta, \phi)]^2 - \sqrt{\text{Ta}} \mathbf{e}_z \times \mathbf{U} + A \cdot T r \sin \theta \mathbf{s}, \tag{22}$$

$$\frac{\partial T}{\partial t} + (\mathbf{U} \cdot \boldsymbol{\nabla}) T = \nabla^2 T + \frac{\text{Ra}_{\text{E}}}{\text{Ra}_{\text{T}}} [\boldsymbol{\nabla} \upsilon_0(r) + \boldsymbol{\nabla} \upsilon_1 (r, \theta, \phi)]^2, \tag{23}$$

$$\nabla^2 \upsilon_1(r, \theta, \phi) = \frac{B}{1 - B \cdot T} \boldsymbol{\nabla} T \cdot [\boldsymbol{\nabla} \upsilon_0(r) + \boldsymbol{\nabla} \upsilon_1 (r, \theta, \phi)], \tag{24}$$

where $\mathbf{e}_z = \cos\theta \mathbf{e}_r - \sin\theta \mathbf{e}_\theta$, $\mathbf{s} = -(\sin\theta \mathbf{e}_r + \cos\theta \mathbf{e}_\theta)$, $\text{Ra}_{\text{E}} = \frac{2\epsilon_0 \epsilon_r \gamma}{\rho \nu \kappa} V_{\text{rms}}^2 \Delta T$ is the Rayleigh number, $\text{Ta} = (\frac{2\Omega d^2}{\nu})^2$ is the Taylor number, $\text{Ra}_{\text{T}} = \frac{c_p \gamma \Delta T^2}{\pi \nu f h_{\text{diss}}}$, $A = \frac{\alpha \Delta T}{4} \text{PrTa}$, $B = \gamma \Delta T$. The boundary conditions for the velocity field $\mathbf{U}$, the temperature T and the electric potential υ_1 are

$$\mathbf{U} = 0, \quad T = 1, \quad \upsilon_1 = 0 \tag{25}$$

on the $r = \eta/(1 - \eta)$ and

$$\mathbf{U} = 0, \quad T = 0, \quad \upsilon_1 = 0 \tag{26}$$

on the $r = 1/(1 - \eta)$. Note that parameters Ra_{T} and B does not change at fixed ΔT. The parameter A depends only on the Taylor number (for fixed Prandtl number). Hence, we can investigate convective flow that depends on the Rayleigh number (or voltage V_{rms}) and the Taylor number (or rotation rate Ω). We list the values of constants for the working fluid 1-Nonanol in this study used in Table I.

III. NUMERICAL METHOD

The fully three-dimensional pseudospectral numerical code for the spherical geometry was developed by Hollerbach [18]. The poloidal-toroidal representation of the velocity field

$$\mathbf{U} = \boldsymbol{\nabla} \times \boldsymbol{\nabla} \times (\Phi \mathbf{e}_r) + \boldsymbol{\nabla} \times (\Psi \mathbf{e}_r) \tag{27}$$
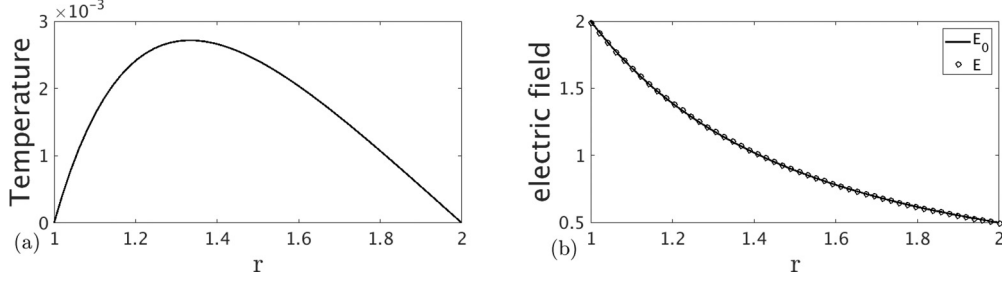
FIG. 1. The base temperature (a) and the base electric field (b) for $\eta = 0.5$, $\Delta T = 0$ K, $R_H = 1.605 \times 10^6$.

automatically obeys the continuity equation. Separated equations for poloidal Φ and toroidal Ψ potentials can be obtained applying operators $\nabla \times \nabla \times$ and $\nabla \times$, correspondingly. After the mapping $r = \frac{1}{2}[z + \frac{1+\eta}{1-\eta}]$ is performed, where $z \in [-1, +1]$, each scalar function can be expanded in terms of the Chebyshev polynomials in the radial direction and in terms of spherical harmonics, $Y_\ell^m(\theta, \phi)$, according to

$$\Phi(t, r, \theta, \phi) = \sum_{m=0}^{MU} \sum_{\ell=\ell'}^{LU} \sum_{k=1}^{KU+4} [f_{ck\ell m}(t) \cos(m\phi) + f_{sk\ell m}(t) \sin(m\phi)] T_{k-1}(z) P_\ell^m(\cos\theta), \quad (28)$$

$$\Psi(t, r, \theta, \phi) = \sum_{m=0}^{MU} \sum_{\ell=\ell'}^{LU} \sum_{k=1}^{KU+2} [e_{ck\ell m}(t) \cos(m\phi) + e_{sk\ell m}(t) \sin(m\phi)] T_{k-1}(z) P_\ell^m(\cos\theta), \quad (29)$$

$\ell' = \max(1, m)$. A similar expression is valid for the temperature

$$T(t, r, \theta, \phi) = \sum_{m=0}^{MT} \sum_{\ell=m}^{LT} \sum_{k=1}^{KT+2} [t_{ck\ell m}(t) \cos(m\phi) + t_{sk\ell m}(t) \sin(m\phi)] T_{k-1}(z) P_\ell^m(\cos\theta). \quad (30)$$

Twenty Chebyshev polynomials ($KU = KT = 20$) and 30 Legendre polynomials ($LU = LT = 30$) were enough to get the grid-independent solution for the two-dimensional basic flow and linear onset calculations for all Taylor numbers and Rayleigh numbers considered. Whereas the same resolution in the radial direction was used for the fully three-dimensional calculations, a values of LU, LT vary between 30 and 40 and MU and MT alter between 20 and 40. The time-dependent spectral coefficients have been calculated by means of the predictor-corrector method. Because we deal with the oscillating bifurcation the perturbed flow depends on time in contrast to the steady two-dimensional basic flow. Therefore, we use such a time step Δt that for all smaller Δt no changes in critical Rayleigh number and drift velocity occur. This time step depends on the Taylor number and varies between $\Delta t = 10^{-4}$ and $\Delta t = 2 \times 10^{-5}$.

IV. BASIC FLOW

From Eqs. (12)–(19) and Eqs. (2), (21)–(24) it follows that the electric field is coupled *directly* not only with the velocity field due to the buoyancy term in the Navier-Stokes equation but also with the temperature, due to the dielectrical heating in the energy equation. This means that the model

under investigation differs from other cases in the literature where the dielectrical heating or other kinds of heating are negligible. This fact makes it slightly complicated to calculate the basic state. In the case of pure heating ($\Delta T = 0$ K), the basic flow is zero in the nonrotating case. To find the temperature, Eq. (14) must be solved numerically together with the Gauss equation, Eq. (15). The base temperature $T_0(r)$ and the base electric field $\mathbf{E}(r) = \mathbf{E}_0(r) + \mathbf{E}_1(r)$ have a radial one-dimensional structure, see Figs. 1(a) and 1(b),

$$\nabla^2 T_0(r) = -\frac{R_H}{R_T}[\nabla v_0(r) + \nabla v_1(r)]^2, \quad (31)$$

$$\nabla^2 v_1(r) = \frac{\gamma T_b}{1 - \gamma T_b T} \nabla T_0(r) \cdot [\nabla v_0(r) + \nabla v_1(r)]. \quad (32)$$

However, in the case of purely dielectrical heating, an additional field $\mathbf{E}_1(r)$ has such a small value [Fig. 1(b)] that it does not influence the temperature. Therefore, the base temperature can be calculated analytically,

$$T_{0I}(r) = -\frac{1}{2} \frac{R_H}{R_T} \frac{\eta^2}{(1-\eta)^4} \left[\frac{(1-\eta)^2}{\eta} - \frac{(1-\eta^2)}{\eta} \frac{1}{r} + \frac{1}{r^2} \right]. \quad (33)$$

The analytical form of the temperature is particularly useful for calculating the Nusselt number of the basic state, defined as follows:

$$Nu_{in0}^{analyt} = \int_{S_{in}} \frac{dT_{0I}(r)}{dr} dS_{in}, \quad (34)$$

$$Nu_{out0}^{analyt} = -\int_{S_{out}} \frac{dT_{0I}(r)}{dr} dS_{out}, \quad (35)$$

where $dS_{in,out} = r_{in,out}^2 \sin\theta d\theta d\phi$. After a little algebra, we obtain

$$Nu_{in0}^{analyt} = Nu_{out0}^{analyt} = \frac{2\pi\eta}{(1-\eta)^2} \frac{R_H}{R_T}. \quad (36)$$

The energy balance equation in terms of the Nusselt number reads

$$-Nu_{in0}^{analyt} - Nu_{out0}^{analyt} + \frac{R_H}{R_T} \int_V E_0^2 dV = 0, \quad (37)$$

i.e., the energy is produced due to the dielectrical heating and leaves the domain under consideration through the inner and outer surfaces.

In the second case ($\Delta T > 0$) without rotation (Ta = 0) and neglecting $\mathbf{E}_1(r)$ the analytical solution for the temperature
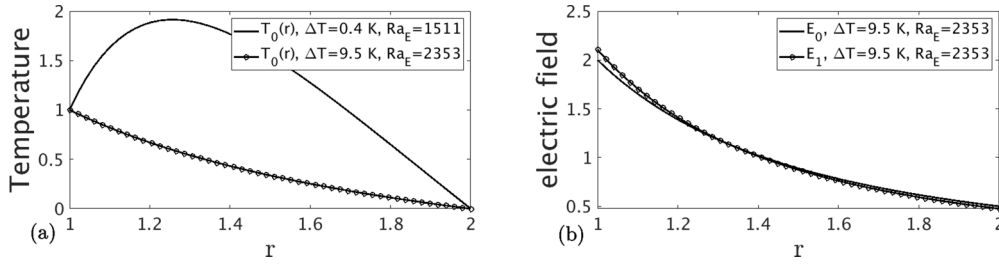
FIG. 2. The basic temperature (a) and the electric field (b) for $\eta = 0.5$.

is

$$T_{0II}(r) = -\frac{\eta}{1-\eta} + \frac{\eta}{(1-\eta)^2}\frac{1}{r}$$
$$-\frac{1}{2}\frac{\mathrm{Ra_E}}{\mathrm{Ra_T}}\frac{\eta}{(1-\eta)^2} + \frac{1}{2}\frac{\mathrm{Ra_E}}{\mathrm{Ra_T}}\frac{\eta(1+\eta)}{(1-\eta)^3}\frac{1}{r}$$
$$-\frac{1}{2}\frac{\mathrm{Ra_E}}{\mathrm{Ra_T}}\frac{\eta^2}{(1-\eta)^4}\frac{1}{r^2}. \tag{38}$$

Note that the solution can be divided into two parts. The first part occurs because the inner surface is warmer than the outer and is responsible for the energy transport from the warmer inner surface into the volume entirely due to conduction. The second one is associated with dielectrical heating ($\sim\frac{\mathrm{Ra_E}}{\mathrm{Ra_T}}$). Two examples of the base temperature are presented in Fig. 2(a). Whereas the influence of the dielectrical heating is particularly significant for small ΔT ($\mathrm{Ra_T} = 138.28$ for $\Delta T = 0.4\mathrm{K}$), conduction prevails for large ΔT ($\mathrm{Ra_T} = 78\,000$ for $\Delta T = 9.5\mathrm{K}$). Both effects influence heat transfer, which can be expressed in the following form in terms of the Nusselt number:

$$\mathrm{Nu}_{in0}^{\mathrm{analyt}} = -\int_{S_{in}}\frac{dT_{0II}(r)}{dr}dS_{in}, \quad \frac{\mathrm{Ra_E}}{2\mathrm{Ra_T}} \leqslant 1, \tag{39a}$$

$$\mathrm{Nu}_{in0}^{\mathrm{analyt}} = \int_{S_{in}}\frac{dT_{0II}(r)}{dr}dS_{in}, \quad \frac{\mathrm{Ra_E}}{2\mathrm{Ra_T}} \geqslant 1, \tag{39b}$$

$$\mathrm{Nu}_{out0}^{\mathrm{analyt}} = -\int_{S_{out}}\frac{dT_{0II}(r)}{dr}dS_{out}. \tag{39c}$$

Hence, whereas the energy flux through the outer surface does not change its sign, the definition of $\mathrm{Nu}_{in0}^{\mathrm{analyt}}$ depends upon which effect is stronger, the dielectrical heating, associated with the imposed electrical field, or the energy transfer because of the conduction. The Nusselt number can be calculated analytically, as in the case of purely dielectrical heating

$$\mathrm{Nu}_{in0}^{\mathrm{analyt}} = \frac{4\pi\eta}{(1-\eta)^2}\left(1-\frac{1}{2}\frac{\mathrm{Ra_E}}{\mathrm{Ra_T}}\right), \frac{\mathrm{Ra_E}}{2\mathrm{Ra_T}} < 1, \tag{40a}$$

$$\mathrm{Nu}_{in0}^{\mathrm{analyt}} = \frac{4\pi\eta}{(1-\eta)^2}\left(\frac{1}{2}\frac{\mathrm{Ra_E}}{\mathrm{Ra_T}}-1\right), \frac{\mathrm{Ra_E}}{2\mathrm{Ra_T}} > 1, \tag{40b}$$

$$\mathrm{Nu}_{out0}^{\mathrm{analyt}} = \frac{4\pi\eta}{(1-\eta)^2}\left(1+\frac{1}{2}\frac{\mathrm{Ra_E}}{\mathrm{Ra_T}}\right). \tag{40c}$$

The energy balance equation in terms of the Nusselt number reads

$$\mathrm{Nu}_{in0}^{\mathrm{analyt}} - \mathrm{Nu}_{out0}^{\mathrm{analyt}} + \frac{\mathrm{Ra_E}}{\mathrm{Ra_T}}\int_V E_0^2\,dV = 0 \tag{41}$$

$$\frac{\mathrm{Ra_E}}{2\mathrm{Ra_T}} < 1,$$

$$-\mathrm{Nu}_{in0}^{\mathrm{analyt}} - \mathrm{Nu}_{out0}^{\mathrm{analyt}} + \frac{\mathrm{Ra_E}}{\mathrm{Ra_T}}\int_V E_0^2\,dV = 0 \tag{42}$$

$$\frac{\mathrm{Ra_E}}{2\mathrm{Ra_T}} > 1.$$

If $\mathrm{Ra_E}/2\mathrm{Ra_T} < 1$, then the heat flux caused by conduction prevails and the system obtains more energy than it loses because of the internal heating. This situation changes if the Rayleigh number exceeds $2\mathrm{Ra_T}$ (e.g., $2\mathrm{Ra_T} = 276.55$ if $\Delta T = 0.4\,K$). Therefore, the Nusselt number has the V-shaped structure.

The influence of $\mathbf{E}_1(r)$ becomes important for large values of ΔT, e.g., $\Delta T = 9.5$ K. The difference between $\mathbf{E}(r)$ and $\mathbf{E}_0(r)$ has a value of 5% at the vicinity of the inner surface [Fig. 2(b)]. Taking $\mathbf{E}_1(r)$ into account decreases the critical Rayleigh number from $\mathrm{Ra_{EcL}} = 2487$ (if the field $\mathbf{E}(r) = \mathbf{E}_0(r)$ is considered) to $\mathrm{Ra_{EcL}} = 2353.29$.

The situation becomes much more complex if the spherical system is rotating (Ta > 0). The centrifugal force causes a two-dimensional axisymmetrical and equatorially symmetrical steady basic flow [$\mathbf{U}_0(r,\theta)$] that must be calculated numerically. Some examples of the basic flow are presented in Fig. 3 in terms of the stream function χ that is connected with velocity components according to $U_{0r}(r,\theta) = \frac{1}{r^2\sin\theta}\frac{\partial\chi}{\partial\theta}$, $U_{0\theta}(r,\theta) = -\frac{1}{r\sin\theta}\frac{\partial\chi}{\partial r}$. The basic flow is presented for the experimentally relevant radii ratio $\eta = 0.5$, Prandtl number Pr = 176, $\Delta T = 0.4$ K, $\Delta T = 1.7$ K, $\Delta T = 3$ K, and for Taylor numbers Ta = 17\,200 and Ta = 68\,800; see Sec VIC. The first row shows the meridional flow or the stream function, the second one depicts the angular velocity and the third row is the temperature. All flows are presented at the critical Rayleigh number $\mathrm{Ra_E} = \mathrm{Ra_{EcL}}$.

If ΔT increases, then the centrifugal force becomes more and more important and the meridional flow [Figs. 3(a)–3(f), first row] concentrates in the vicinity of the inner surface. The main part of the angular velocity field [Figs. 3(a)–3(f), second row] concentrates near the inner surface, building the boundary layer. The maximum temperature [Figs. 3(a)–3(f), third row] is located within the gap, emphasizing the importance of the internal heating. These features of the basic flow are
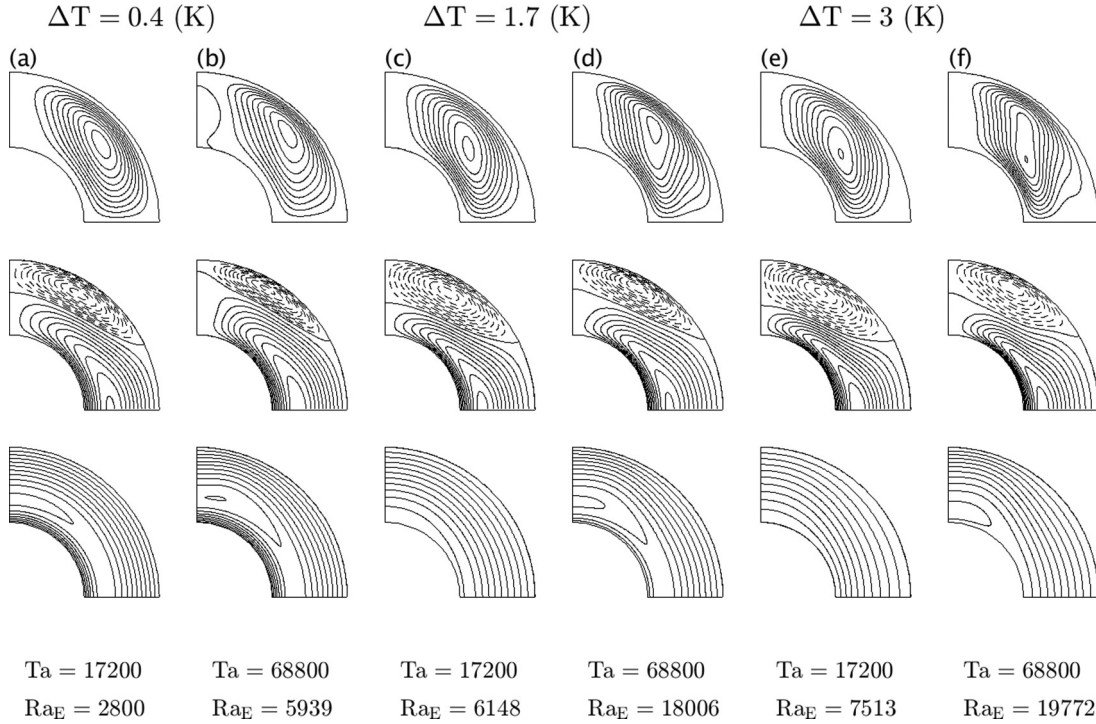
$\Delta T = 0.4$ (K) $\Delta T = 1.7$ (K) $\Delta T = 3$ (K)

(a)   (b)   (c)   (d)   (e)   (f)

| Ta = 17200 | Ta = 68800 | Ta = 17200 | Ta = 68800 | Ta = 17200 | Ta = 68800 |
| Ra$_E$ = 2800 | Ra$_E$ = 5939 | Ra$_E$ = 6148 | Ra$_E$ = 18006 | Ra$_E$ = 7513 | Ra$_E$ = 19772 |

FIG. 3. Basic flow (presented at the critical Ra$_{EcL}$): first row contours of the meridional circulation χ with (a) $\chi_{max} = 0.36$, (b) $\chi_{max} = 0.9$, (c) $\chi_{max} = 0.48$, (d) $\chi_{max} = 0.96$, (e) $\chi_{max} = 0.76$, (f) $\chi_{max} = 1.2$. Second row contours of the angular velocity with maximal and minimal values (a) $+2.8$, -1.2, (b) $+12.6$, -4.8, (c) 3.6, -2, (d) $+14$, -6.4, (e) $+5$, -3.42, (f) $+15$, -8.0. Third row contours of the temperature with (a) $T_{max} = 3.1$, (b) $T_{max} = 6.4$, (c) $T_{max} = 1.0$, (d) $T_{max} = 1.6$, (e) $T_{max} = 1.0$, (f) $T_{max} = 1.05$.

crucial for understanding of the origin of the instability as discussed in the next section.

The Nusselt number can be calculated numerically only in the rotating case because of the existence of the basic flow. We present the Nusselt number as a function of Ra$_E$ (Fig. 4) for fixed Taylor number Ta $= 17\,200$. The shape of the Nu$_{in0}$(Ra$_E$), corresponding to the heat transfer through the inner surface in the case of the basic flow (for the fixed $\Delta T = 0.4$ K and $\Delta T = 1.7$ K) is similar to the nonrotating case. Interestingly, the zero-flux point, Ra$_{E0}$, in which Nu$_{in0} = 0$, i.e., heat fluxes produced due to the imposed electrical field and applied ΔT are the same, almost coincides with 2Ra$_T$ for $\Delta T = 0.4$ K (Ra$_{E0} = 276.27$, 2Ra$_T = 276.55$) and differs only slightly within a range of 0.5% for $\Delta T = 1.7$ K (Ra$_{E0} = 5016$, 2Ra$_T = 4995.27$). Whereas Nu$_{out0}$(Ra$_E$) can be approximated by means of linear law [Eq. (40c)] with very good accuracy (less than 0.01%) for $\Delta T = 0.4$ K and

$\Delta T = 1.7$ K, Eqs. (40a) and (40b) can be used to calculate the value Nu$_{in0}$(Ra$_E$) only for $\Delta T = 0.4$ K. Detailed analysis shows that numerically obtained Nusselt number, Nu$_{in0}$(Ra$_E$), can be approximated by (Fig. 4, left)

$$\text{Nu}_{in0}^{approx} = -0.005025\text{Ra}_E + 25.20, \frac{\text{Ra}_E}{\text{Ra}_{E0}} < 1, \quad (43)$$

$$\text{Nu}_{in0}^{approx} = 0.004989\text{Ra}_E - 25.03, \frac{\text{Ra}_E}{\text{Ra}_{E0}} > 1 \quad (44)$$

for $\Delta T = 1.7$ K.

If the ΔT increases, then the zero-flux point Ra$_{E0}$ does not occur because the heat flux due to conduction through the inner surface prevails over the heat flux caused by the source H_E. Therefore, the Nusselt number for $\Delta T = 3$ K and Ta $= 17\,200$ must be calculated numerically and the analytically obtained expressions Eqs. (40a)–(40c) are no longer valid.
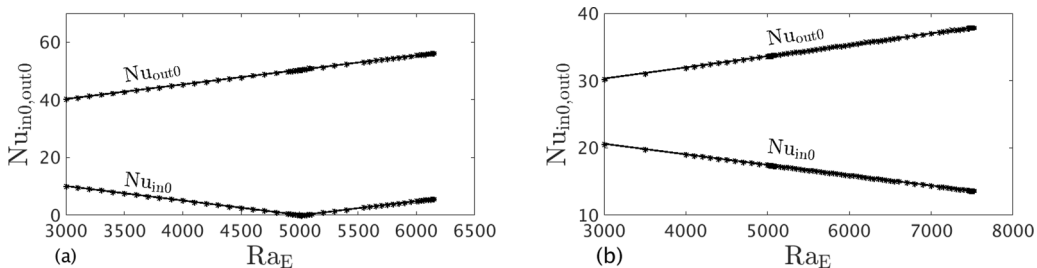

FIG. 4. Nusselt number vs. Rayleigh number for $\Delta T = 1.7$ K (a) and $\Delta T = 3.0$ K (b), $\eta = 0.5$ and Ta $= 17\,200$. Numerically obtained Nusselt number is presented in solid, the approximated Nusselt number Eqs. (44)–(47) is presented with stars.
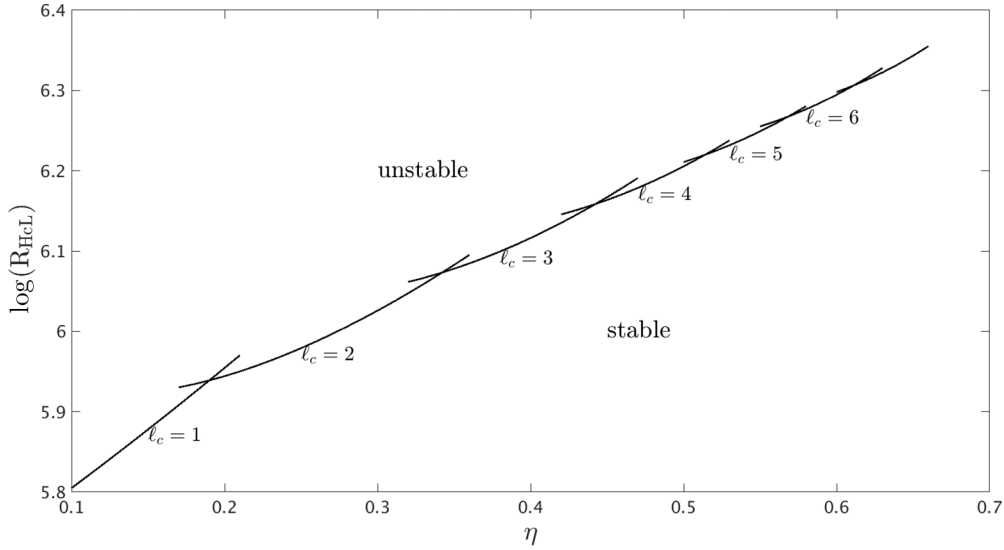
FIG. 5. Critical Rayleigh-Roberts numbers in the case of purely dielectrical heating ($\Delta T = 0$ K).

Nevertheless, numerically obtained Nusselt number can be approximated according to (Fig. 4, right).

$$\mathrm{Nu}_{\mathrm{in0}}^{\mathrm{approx}} = -0.001537 \mathrm{Ra}_{\mathrm{E}} + 25.17, \tag{45}$$

$$\mathrm{Nu}_{\mathrm{out0}}^{\mathrm{approx}} = 0.001694 \mathrm{Ra}_{\mathrm{E}} + 25.17. \tag{46}$$

V. LINEAR INSTABILITY ANALYSIS

Stability of the basic flow was investigated in frames of linear theory. This is a useful tool to derive such critical Rayleigh-Roberts, $\mathrm{R}_{\mathrm{HcL}}$, or Rayleigh number, $\mathrm{Ra}_{\mathrm{EcL}}$, above which the basic flow becomes unstable with respect to infinitesimal perturbations **u** for the velocity, Θ for the temperature, $\tilde{p}$ for the pressure, and $\tilde{\upsilon}$ for the electric potential. Because of the continuity Eq. (8) the poloidal-toroidal decomposition Eq. (27) can be used for the field **u**,

$$\mathbf{u} = \nabla \times \nabla \times (\tilde{\Phi}\mathbf{e}_r) + \nabla \times (\tilde{\Psi}\mathbf{e}_r), \tag{47}$$

too. Furthermore, the expressions Eqs. (28)–(30) are valid for the perturbations in which the spectral coefficients, e.g., $f_{ck\ell m}$ have been replaced by $\tilde{f}_{ck\ell m}$. The eigenvalue problem was solved by means of direct numerical integration. Because the basic flow is steady the temporal structure of the solution of the linearized equation system has form of $e^{\sigma t}$, where $\sigma = \zeta + i\omega$ is the dominant eigenvalue, the real part of the eigenvalue ζ is the growth rate, and ω is the frequency of the perturbation. The goal of the linear analysis is to find such value of the control parameter ($\mathrm{R}_{\mathrm{HcL}}$ and $\mathrm{Ra}_{\mathrm{EcL}}$) at which $\zeta = 0$. Frequency ω defines a kind of bifurcation. If $\omega = 0$, then the basic flow becomes unstable with respect to the stationary perturbations. If $\omega > 0$, then the instability sets in as an oscillating bifurcation.

A. Nonrotating case

Note that the linearized equations, formulated in the spectral space, do not depend on the azimuthal wave number m in the nonrotating case. Furthermore, the linear instability equations can be separated for each number ℓ. Numerical

analysis shows that the basic flow becomes unstable with respect to steady perturbations for all radius ratios considered, i.e., $\omega = 0$. This numerical result is in accordance with the analytical results obtained for the case of the plane and cylindrical geometries [19–21]. The growth rate is calculated according to $\sigma = \frac{1}{\Delta t} \ln \frac{|g_{k\ell}(t+\Delta t)|}{|g_{k\ell}(t)|}$, where $g_{k\ell}(t)$ is the arbitrary spectral coefficient ($\tilde{f}_{c,s}$ or $\tilde{t}_{c,s}$) with fixed subscript k and tested number ℓ. Note that in the linear approach the toroidal potential vanishes $\tilde{\Psi} = 0$ in the nonrotating case. The critical Rayleigh-Roberts number and the critical Rayleigh number, defined as

$$\mathrm{R}_{\mathrm{HcL}}(\eta) = \min_{\ell} \mathrm{R}_{\mathrm{H}}(\ell, \eta), \quad \mathrm{Ra}_{\mathrm{EcL}}(\eta) = \min_{\ell} \mathrm{Ra}_{\mathrm{E}}(\ell, \eta), \tag{48}$$

obey $\sigma = 0$.

Critical Rayleigh-Roberts numbers for the case of purely dielectric heating are presented in Fig. 5. We see that the critical Rayleigh-Roberts number is $\mathrm{R}_{\mathrm{HcL}} = 1.6049 \times 10^6$, which corresponds to the voltage $V_{\mathrm{rms,crit.}} = 1754$ V. The critical wave number is $\ell_c = 4$. The influence of the imposed ΔT is presented in Fig. 6. Although the critical Rayleigh number increases from $\mathrm{Ra}_{\mathrm{EcL}} = 1511.32$ for $\Delta T = 0.4$ K to $\mathrm{Ra}_{\mathrm{EcL}} = 2411.29$ for $\Delta T = 3$ K, the corresponding values of the voltage decrease drastically from $V_{\mathrm{rms,crit.}} = 1456$ V to $V_{\mathrm{rms,crit.}} = 671$ V. Hence, increasing ΔT destabilizes the basic state: A lower voltage is needed for the transition into the three-dimensional flow.

B. Rotating case

If the spherical system rotates with the rotation rate Ω, then the Coriolis force and the centrifugal force must be taken into account. Additionally to the Rayleigh number Ra_{E}, the flow is characterized by the Taylor number, Ta, and the parameter $A = \frac{1}{4}\alpha\Delta T \mathrm{PrTa}$. As in the nonrotating case, the linearized Navier-Stokes equation, the energy equation and the Gauss equation were solved directly to derive the critical Rayleigh number. The basic feature of the equations, describing the
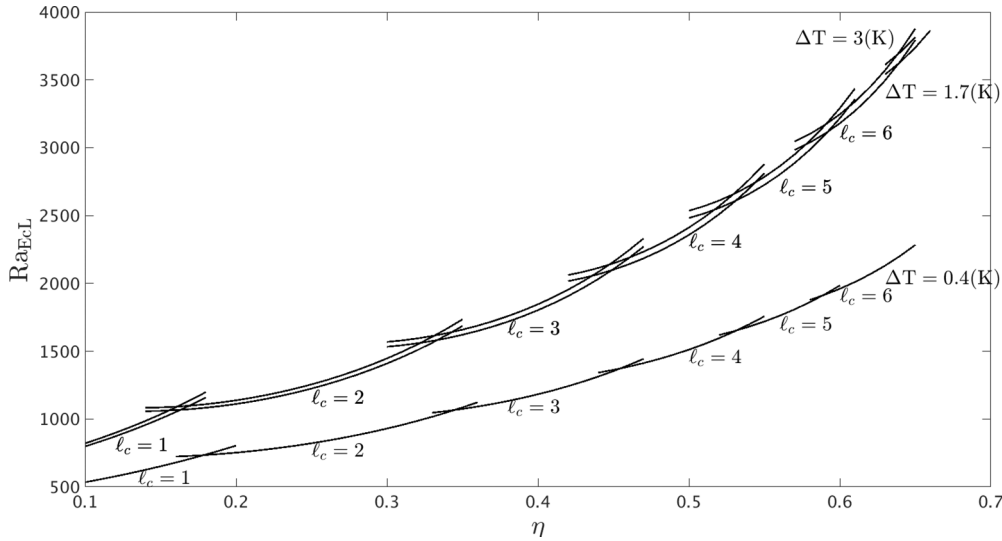
FIG. 6. Critical Rayleigh numbers for the dielectrical heating and $\Delta T > 0$.

stability problem, is that they can be formulated for each azimuthal wave number m. In other words, we have to solve M two-dimensional problems, where M is the maximum of the all wave numbers under consideration. Furthermore, because of the equatorial symmetry of the basic flow, the linear system of equations to be solved can be divided into two sets, corresponding to the two symmetry classes. Perturbations of the first class satisfy the relation

$$\{u_r, u_\theta, u_\phi, \Theta\}(r, \theta, \phi) = \{u_r, -u_\theta, u_\phi, \Theta\}(r, \pi - \theta, \phi),$$
(49)

which is symmetric with respect to the equator, and perturbations of the second class,

$$\{u_r, u_\theta, u_\phi, \Theta\}(r, \theta, \phi) = \{-u_r, u_\theta, -u_\phi, -\Theta\}(r, \pi - \theta, \phi),$$
(50)

are equatorially antisymmetric.

The *first* class is responsible for the instability of the problem under consideration. The critical Rayleigh number is calculated according to

$$\mathrm{Ra_{EcL}(Ta)} = \min_m \mathrm{Ra_E}(m, \mathrm{Ta})$$
(51)

for the fixed Prandtl number and radii ratio η.

Unfortunately, far more numerical effort is needed to perform the stability analysis in the rotating case in contrast to the nonrotating case considered above. Therefore, we limit the stability investigations to cases with $\eta = 0.5$, $\mathrm{Pr} = 176$, $\Delta T = 0.4$ K, $\Delta T = 1.7$ K, and $\Delta T = 3$ K, which are relevant for the GeoFlow experiment. The critical Rayleigh numbers as a function of the Taylor number are presented in Fig. 7. The basic flow becomes unstable with respect to the nonaxisymmetric perturbations with $m_c > 0$: the critical
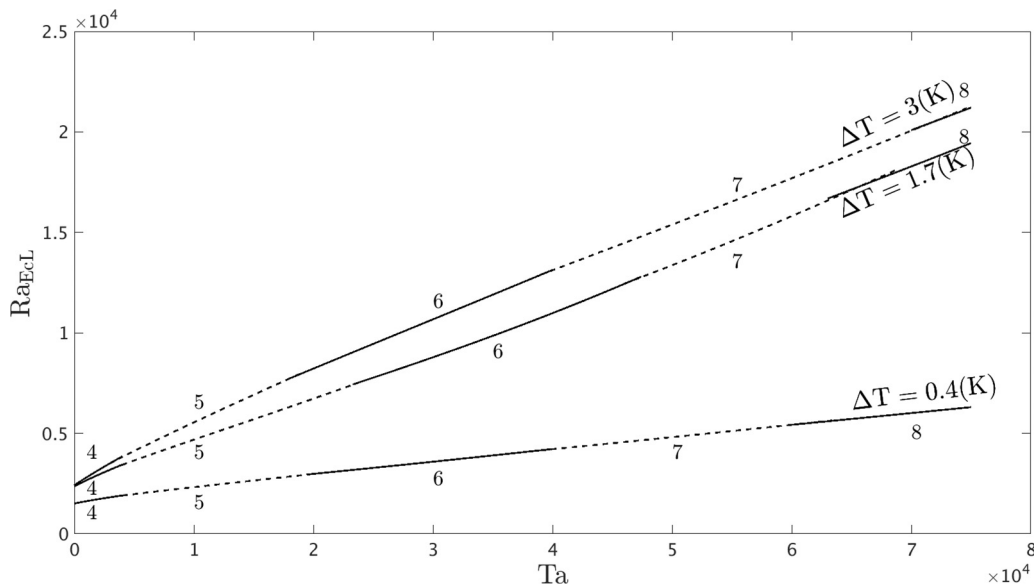

FIG. 7. Critical Rayleigh numbers vs. Taylor number for $\eta = 0.5$ and $\mathrm{Pr} = 176$. The numbers in the vicinity of the stability curves are the critical azimuthal wave numbers m_c.
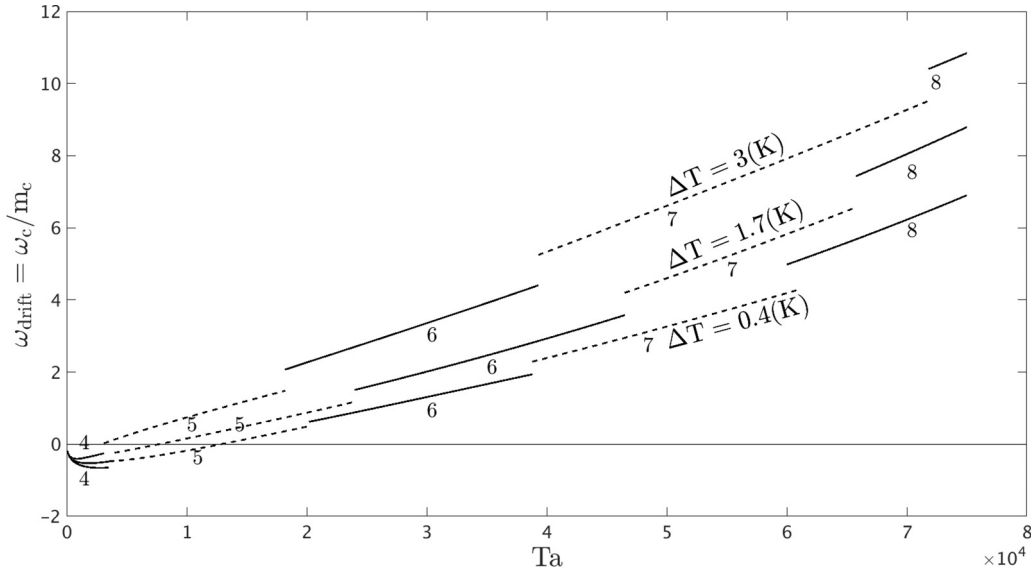
FIG. 8. Drift velocity vs. Taylor number. The numbers in the vicinity of the drift velocity curves are the critical azimuthal wave numbers m_c.

azimuthal wave number varies between $m_c = 4$ for small Taylor numbers and $m_c = 7, 8$ for Taylor numbers in the order of 10^4. Note that for $\mathrm{Ta} > 2.0 \times 10^4$ the critical Rayleigh number can be be approximated according to linear law, i.e., $\mathrm{Ra_{EcL}} \sim \mathrm{Ta}$. The instability sets in as an oscillating bifurcation. The perturbative flow drifts with a velocity (Fig. 8) of $\omega_{\mathrm{drift}} = \omega_c / m_c$, where ω_c is the frequency of the dominant perturbation, corresponding to the wave number m_c. An interesting feature of the drift can be detected for small Taylor numbers. Whereas the spherical gap rotates counterclockwise, the perturbative flow drifts clockwise (Fig. 8). An increase in Ta leads to the change of direction and the higher magnitude of the drift velocity.

It is useful to express the nondimensional parameters such as the Rayleigh number, Taylor number, and drift velocity, ω_{drift}, in terms of the voltage, V_{rms}, rotation rate Ω, and $\omega_{\mathrm{drift}}^{\mathrm{dim}}$ (Table II). This makes it more convenient to compare the results with the GeoFlow experiment. The rotation has a strongly stabilizing effect: If the Taylor number rises, then there is an increase in the critical voltage at which the transition from the basic flow into the three-dimensional flow occurs. The drift velocity of the perturbation $\omega_{\mathrm{drift}}^{\mathrm{dim}}$ is much lower than the rotation rate Ω.

The next issue is to follow why and where the instability occurs. Although the instability can be located by calculating

the eigenvectors, i.e., the velocity field, corresponding to $\mathrm{Ra_{EcL}}$, it can also be located using the azimuthally integrated kinetic energy of the perturbation $e(r, \theta) = \frac{1}{2} \int \mathbf{u}^2 r \sin \theta \, d\phi$, which is a more convenient tool for analyzing the origin of the instability (Fig. 9). It is important to note that although we deal with the oscillatory bifurcation, the kinetic energy of the perturbative flow remains constant. Therefore, one snapshot is sufficient to determine that there are two regions where the instability concentrates. The first one is the shear instability that appears within the meridional flow (Fig. 9). In the next section we will see that the radial and the longitudinal velocity components of the perturbation are responsible for this instability. The second one occurs in the vicinity of the equator and is associated with the azimuthal velocity component. Although it is impossible to derive amplitudes of the supercritical flow in frames of the linear stability analysis, we are able to predict its patterns. An example of the critical perturbation with $m_c = 5$ is presented in Fig. 10.

VI. THREE-DIMENSIONAL ANALYSIS

Besides the linear instability analysis, we present also simulations of the nonlinear three-dimensional flow. Because the computational effort increases considerably with $\mathrm{Ra_E}$, we consider only slightly supercritical states.

TABLE II. Connection between nondimensional characteristics ($\mathrm{Ra_{EcL}}$, ω_{drift}) of the instability and dimensional characteristics (V_{rms}, $\omega_{\mathrm{drift}}^{\mathrm{dim}}$). m_c indicate the critical azimuthal wave numbers.

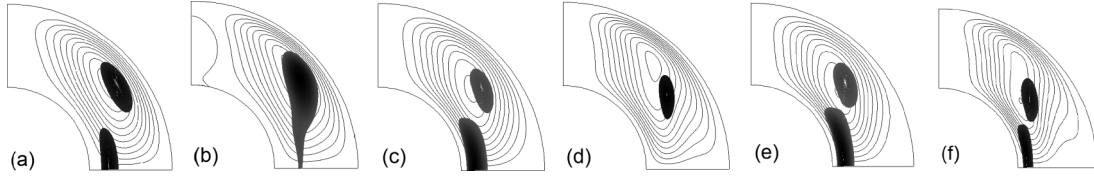| ΔT (K)	Ta	Ω (s^{-1})	$\mathrm{Ra_{EcL}}$	$V_{\mathrm{rms,crit.}}$ (V)	m_c	ω_{drift}	$\omega_{\mathrm{drift}}^{\mathrm{dim}}$ (s^{-1})
0.4	17 200	0.8	2 800	1 982	5	0.2901	1.264×10^{-4}
0.4	68 800	1.6	5 940	2 887	8	6.067	2.643×10^{-3}
1.7	17 200	0.8	6 149	1 425	5	0.6670	2.905×10^{-4}
1.7	68 800	1.6	18 006	2 438	8	7.868	3.428×10^{-3}
3	17 200	0.8	7 513	1 186	5	1.394	6.073×10^{-4}
3	68 800	1.6	19 773	1 923	7	9.104	9.325×10^{-3}

FIG. 9. As in Figs. 3(a)–3(f), the basic meridional circulation is shown. The gray shading indicates the location of the azimuthally integrated kinetic energy $e(r, \theta)$ of the perturbation. Both the basic meridional circulation and $e(r, \theta)$ are shown at the critical Rayleigh number.

The goals of the three-dimensional investigation are as follows. First, we check the results of the linear instability analysis. If the Rayleigh number exceeds the critical value, then the basic flow must become unstable and take on the 3D structure according to the results predicted in the previous section with the same characteristics: ℓ_c in the nonrotating case and m_c and ω_c for Ta > 0. Second, we have to investigate whether we are dealing with subcritical or supercritical bifurcation by analyzing the behavior of the amplitude. The third reason, why the nonlinear equilibration is essential, is the possibility to follow how the internal heating influences the heat transfer.

A. Three-dimensional analysis: Nonrotating case (Ta = 0)

Beginning with the purely dielectrical heating ($\Delta T = 0$ K) without rotation, we choice a total kinetic energy as a control parameter of the supercritical flow. The amplitude a is defined according to

$$a^2 = E = \frac{1}{2} \int_V \mathbf{U}^2 dV = \sum_{\ell=1}^{LU} E_\ell = \sum_{\ell=1}^{LU} \sum_{m=0}^{\ell} \epsilon_{\ell m}. \quad (52)$$

Introducing expressions

$$\hat{f}_{c,s\ell m}[t, r(z)] = \sum_{k=1}^{KU+4} f_{c,sk\ell m}(t) T_{k-1}(z), \quad (53)$$

$$\hat{e}_{c,s\ell m}[t, r(z)] = \sum_{k=1}^{KU+2} e_{c,sk\ell m}(t) T_{k-1}(z), \quad (54)$$

energies $\epsilon_{\ell m}$ have been calculated analytically,

$$
\epsilon_{\ell m}(t) = \left(\ell^2 (\ell+1)^2 \int_{\eta/(1-\eta)}^{1/(1-\eta)} \frac{\hat{f}_{\ell m}^2(t, r)}{r^2} dr \right.
$$
$$
+ \ell(\ell+1) \int_{\eta/(1-\eta)}^{1/(1-\eta)} \hat{e}_{\ell m}^2(t, r) dr
$$
$$
\left. + \ell(\ell+1) \int_{\eta/(1-\eta)}^{1/(1-\eta)} \hat{f}_{\ell m}'^2(t, r) dr \right) C_{\ell m}, \quad (55)
$$

where $\hat{f}_{\ell m}^2(t, r) = \hat{f}_{c\ell m}^2(t, r) + \hat{f}_{s\ell m}^2(t, r)$ [the same relations are valid for $\hat{e}_{\ell m}^2(t, r)$ and $\hat{f}_{\ell m}'^2(t, r)$], and $C_{\ell 0} = \frac{2\pi}{2\ell+1}$ for $m = 0$, $C_{\ell m} = \frac{\pi}{2\ell+1} \frac{(\ell+m)!}{(\ell-m)!}$ for $m > 0$.

The behavior of the amplitude $a^2(R_H)$ for $\eta = 0.5$ and Pr $= 176$ is presented in Fig. 11 (left). According to the three-dimensional calculations, the basic flow suddenly becomes unstable with respect to the infinitesimal perturbations if the Rayleigh number exceeds the critical value $R_H > R_{HcL}$ in agreement with the results given by linear instability theory. If $R_{Hc} < R_H < R_{HcL}$, then the basic flow remains stable regarding small perturbations but becomes unstable with respect to the perturbations with finite amplitude. The transition from the convective branch on the branch, corresponding to the basic state $a = 0$, occurs at $R_{Hc} = 1.566 \times 10^6$. The instability sets in as *subcritical* bifurcation, which causes the hysteresis effect.

Let us consider the bifurcation diagram in detail (Fig. 11, left). The conducting state has been used as the initial condition. Furthermore, the mode corresponding to the critical one is perturbed to obtain the three-dimensional flow. If the Rayleigh-Roberts number is less than $R_H < 1.7 \times 10^6$, then
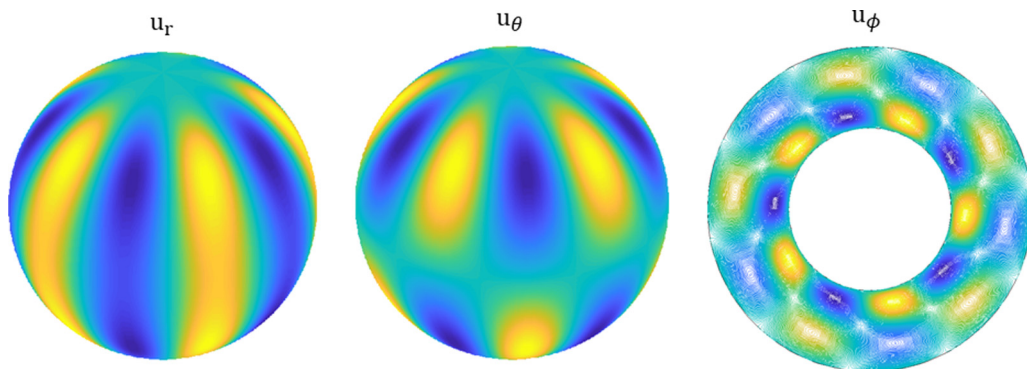

FIG. 10. Velocity components of perturbation u_r, u_θ at $r = 1.6$ and u_ϕ at the equator for $Ra_{EcL} = 2800$, Ta $= 17200$, $\Delta T = 0.4$ K, and $m_c = 5$.
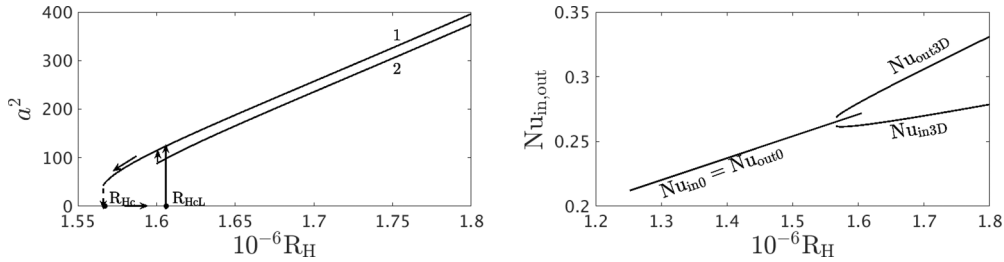
FIG. 11. The bifurcation diagram for the purely dielectrical heating flow is shown left. Arrows detect the hysteresis loop and transition between branches. The Nusselt number behavior is presented right.

we obtain the steady 3D flow in octahedral form (bifurcation branch 1). Starting at $R_H > 1.7 \times 10^6$ we again obtain a steady three-dimensional flow but with a pentagonal structure (bifurcation branch 2). Moving along this branch and decreasing R_H, we jump on the first bifurcation branch at $R_H = 1.6 \times 10^6$. This transition is shown with small arrow. Hence, an important feature of the flow caused by the purely dielectrical heating is the nonuniqueness of the solution. An example of two different flows at $R_H = 1.75 \times 10^6$ is presented in Fig. 12. Energies E_ℓ that make the greatest contribution are listed in Table III.

Note that the mode with $\ell_c = 4$ is dominantly in agreement with linear stability theory. A similar result has been detected in the case of convection ($H_E = 0$) [6].

The heat transfer results are summarized in (Fig. 11, right). Whereas the Nusselt number is the same for the basic flow for both surfaces $Nu_{in0} = Nu_{out0}$, in the three-dimensional case the heat transfer is divided into two branches. Although

the Nusselt number, Nu_{in3D}, increases with Ra_E, the energy flux decreases considerably compared to the basic state. The behavior of the Nu_{out3D} completely differs from Nu_{out0}. The system loses the energy from the outer surface much faster if the flow becomes a three-dimensional structure.

The subcritical bifurcation scenario is detected in the case of convection, also influenced by the dielectrical heating with the applied $\Delta T = 0.4$ K between spherical surfaces (Fig. 13, left). As in the case of the purely dielectrical heating, the basic flow becomes abruptly unstable for $Ra_E > Ra_{EcL} = 1\,511.32$ in accordance with lines stability theory. The three-dimensional flow is stable with the interval $1\,507 = Ra_{Ec} < Ra_E < Ra_{EcL}$. The hysteresis effect is much weaker in contrast to the purely dielectrical heating. Indeed, the difference $\Delta = (Ra_{EcL} - Ra_{Ec})/Ra_{EcL} = 0.26\%$ is much smaller than $\Delta_H = (R_{HcL} - R_{Hc})/R_{HcL} = 2.1\%$ In contrast to the purely dielectrical heating case, only one flow structure, the octahedral structure, is found. The similar Nusselt number shape, corresponding to the three-dimensional flow, has been observed in the convective case (Fig. 13, right).
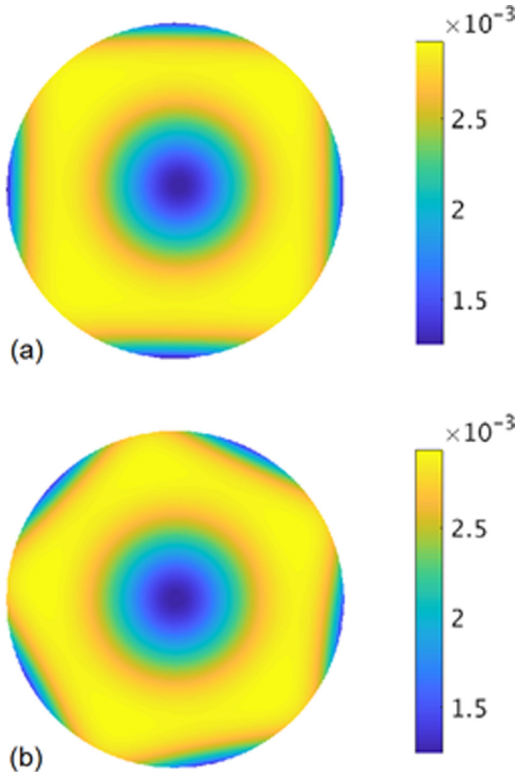
B. Three-dimensional analysis: Rotating case (Ta > 0)

We shall now present the results in the rotating case, comparing them with the results given by linear stability theory. Some examples are shown in Figs. 14(a)–14(c). The longitudinal velocity component of the three-dimensional flow, U_θ, with the $m = 8$ structure is presented in Fig. 14 a for a slightly supercritical Rayleigh number ($Ra_{EcL} = 5904$). The flow drifts with $\omega_{drift}^{3D} = 6.1511$, which is in good agreement with stability results ($\omega_{drift} = 6.0672$). The kinetic energy $E(r, \theta) = \frac{1}{2} \int U^2 r \sin\theta \, d\phi$ [Fig. 15(b) mode $m = 0$, corresponding to the axisymmetric basic flow and nonlinear interactions because of the nonlinear term in the Navier-Stokes equation, is substracted] is concentrated within the meridional flow, confirming the spatial characteristics of the stability analysis [Fig. 9(b)]. Interestingly, the distribution

FIG. 12. Nonuniqueness of the solution: the temperature distribution for $R_H = 1.75 \times 10^6$ at $r = 1.5$.

TABLE III. Most dominant kinetic energies for $\eta = 0.5$, $R_H = 1.75 \times 10^6$, and $Pr = 176$ for the octahedral structure (left) and the pentagonal structure (right).

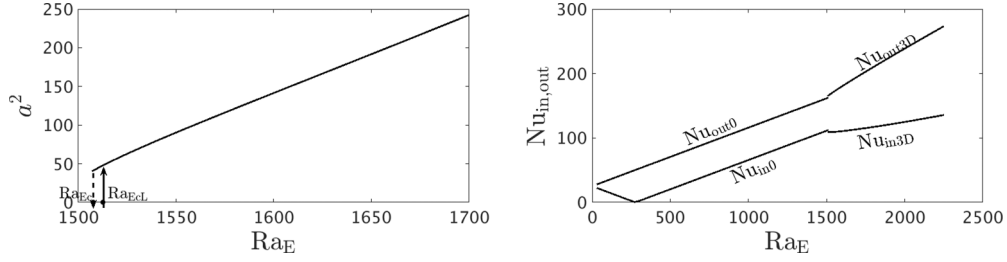| ℓ	E_ℓ	ℓ	E_ℓ
4	299.15	4	186.68
6	18.81	5	101.97
8	8.089	7	8.5822
10	0.1724	8	4.7228

FIG. 13. Left-bifurcation diagram for the flow, caused by the dielectrical heating with convection, right-Nusselt numbers for $\eta = 0.5$ and $\Delta T = 0.4$ K.

of $E(r, \theta)$ ($E_{\max} = 68$) almost coincides with $E_{r\theta}(r, \theta) = \frac{1}{2} \int (U_r^2 + U_\theta^2) r \sin \theta d\phi$ ($E_{r\theta \max} = 66$), emphasizing that the radial and longitudinal velocity components make a most essential contribution into the shear instability.

Two further examples of the supercritical flows are presented in Figs. 14(b) and 14(c). The $m = 5$ and $m = 7$ solutions drift with $\omega_{\text{drift}}^{3D} = 0.6561$ ($\omega_{\text{drift}} = 0.6662$) and $\omega_{\text{drift}}^{3D} = 9.1776$ ($\omega_{\text{drift}} = 9.1044$), correspondingly (Fig. 8). The 3D supercritical solution is symmetrical with respect to the equator and obeys Eq. (50) in accordance with stability results.

The maximum kinetic energy for the $m_c = 5$ solution is now located in the boundary layer in the vicinity of the equator [Fig. 15(c)], which is in accordance with linear stability analysis [Fig. 9(c)]. The instability is associated with the azimuthal component U_ϕ and can be expressed in terms of $E_\phi(r, \theta) = \frac{1}{2} \int U_\phi^2 r \sin \theta d\phi$ ($E_{\max} = 16.5$, $E_{\phi \max} = 14.5$ at the equator).

The kinetic energy for the $m_c = 7$ solution has two maxima [Fig. 15(f)]. Hence, the instability locates in both places described above as linear analysis predicts [Fig. 9(f)]. The corresponding values of the energies are $E_{\max} = 37$, $E_{\phi \max} = 30.5$ at the equator, $E_{\max} = 33.5$, $E_{r\theta \max} = 32.5$ within the meridional flow.

The bifurcation scenario in the rotating case differs from the scenario considered above. Introducing an amplitude according to the expression

$$a^2 = E = \frac{1}{2} \int_V \mathbf{U}^2 dV = \sum_{m=1} E(m) = \sum_{m=1} \sum_{\ell=m} \epsilon_{\ell m} \quad (56)$$

and calculating the amplitude as a function of the supercriticality $\delta = (\text{Ra}_E - \text{Ra}_{\text{EcL}})/\text{Ra}_{\text{EcL}}$, which is more useful as the control parameter in the rotating case, we note that now we are

dealing with the *supercritical* bifurcation. The basic steady flow loses its stability when $\delta > 0$. The amplitude of the supercritical flow can be expressed according to the Landau equation

$$a^2 = C\delta, \quad (57)$$

with $C(\Delta T = 0.4K) = 2420.64$, $C(\Delta T = 1.7K) = 1624.09$, and $C(\Delta T = 3K) = 1892.25$ [Fig. 16(a)].

The Nusselt number shape undergoes a break in the Ra_{EcL}, confirming that the stability results are correct [Figs. 16(b)–16(d)]. The numerically obtained Nusselt numbers $\text{Nu}_{\text{in3D}}(\text{Ra}_E)$ and $\text{Nu}_{\text{out3D}}(\text{Ra}_E)$ can be approximated for the fixed Taylor number $\text{Ta} = 17\,200$ and $\Delta T = 0.4$ K, $\Delta T = 1.7$ K, and $\Delta T = 3$ K as follows:

$$\text{Nu}_{\text{in3D}} = a_{\text{in3D}} \text{Ra}_E + b_{\text{in3D}},$$
$$\text{Nu}_{\text{out3D}} = a_{\text{out3D}} \text{Ra}_E + b_{\text{out3D}}. \quad (58)$$

The constants are presented in Table IV.

C. Comparison with experiment

The critical voltages $V_{\text{rms,crit}}$ are compared with outcomes of the GeoFlow experiment (2008–2018). The experimental setup is based on a spherical capacitor with a radius ratio $\eta = 0.5$, where convective flows are investigated under micro-gravity conditions on the ISS [7,22]. By reason of design constraints, the outer radius of the fluid cell measures 0.027 m and the inner radius 0.0135 m. GeoFlow utilizes the dielectrophoretic force to establish a radial force field with voltages between the minimum value of $V_{\text{rms}} = 1272$ V and the maximum value of $V_{\text{rms}} = 4596$ V. Figure 17 depicts a vertical cut through the GeoFlow experiment. A numerical
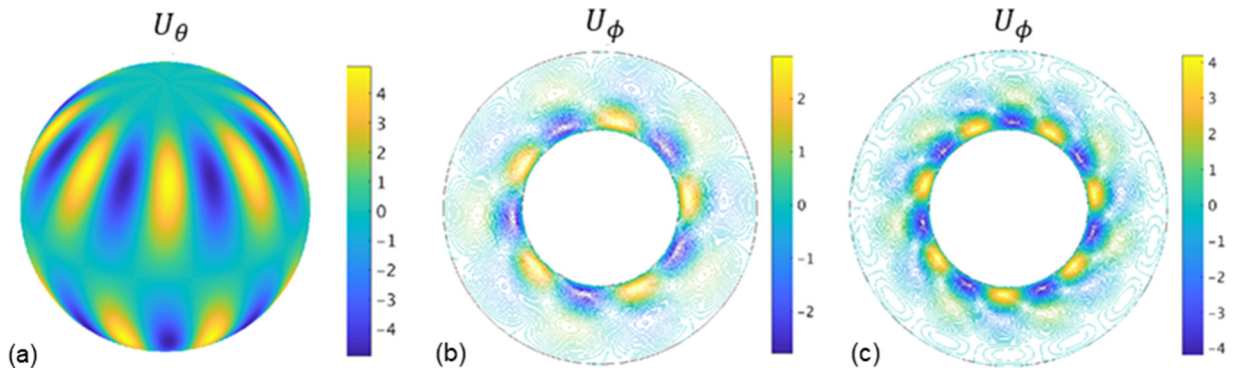

FIG. 14. (a) U_θ at $r = 1.67$ for $\Delta T = 0.4$ K, Ta $= 68\,000$, Ra$_E = 6\,000$; (b, c) U_ϕ at the equator for $\Delta T = 1.7$ K, Ta $= 17\,200$, Ra$_E = 6\,220$ and $\Delta T = 3$ K, Ta $= 68\,800$, Ra$_E = 20\,050$, correspondingly.
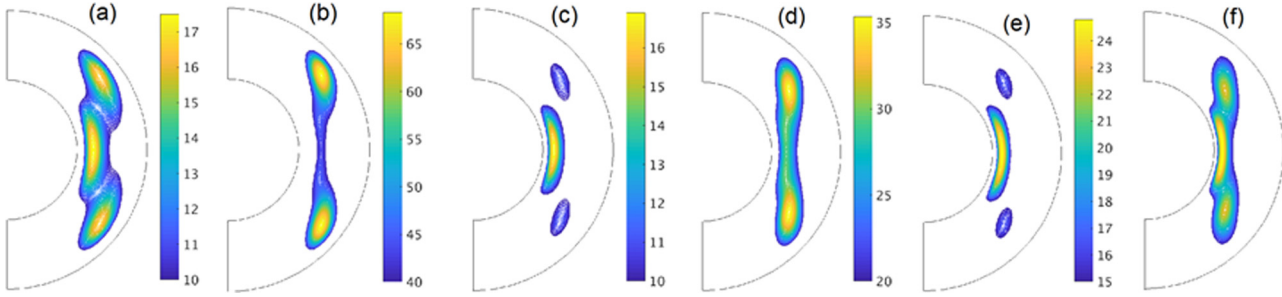
FIG. 15. Azimuthally integrated kinetic energy $E(r, \theta)$ of the three-dimensional flow: (a) $\Delta T = 0.4$ K, Ta $= 17\,200$, $\mathrm{Ra_E} = 2\,830$, (b) $\Delta T = 0.4$ K, Ta $= 68\,800$, $\mathrm{Ra_E} = 6\,000$, (c) $\Delta T = 1.7$ K, Ta $= 17\,200$, $\mathrm{Ra_E} = 6\,220$, (d) $\Delta T = 1.7$ K, Ta $= 68\,800$, $\mathrm{Ra_E} = 18\,200$, (e) $\Delta T = 3$ K, Ta $= 17\,200$, $\mathrm{Ra_E} = 7\,620$, (f) $\Delta T = 3$ K, Ta $= 68\,800$, $\mathrm{Ra_E} = 20\,050$.

simulation visualizes the fluid cell. Heating and cooling circuits thermalize the inner and outer shells, respectively.

The working fluid 1-Nonanol is strongly susceptible to dielectric heating with rates up to 0.1 K/s. The temperature difference across the gap can be adjusted between $0.4\mathrm{K} \leqslant \Delta\mathrm{T} \leqslant 10\mathrm{K}$. In total, 160 experimental points with five different voltages ($V_0 = 1\,800$ V, $3\,000$ V, $4\,200$ V, $5\,400$ V, $6\,500$ V), two reference temperatures ($T_b = 293$ K, 303.5 K) and eight temperature differences (0.4 K $< \Delta T < 9.5$ K) were conducted. Each experimental point was repeated for three rotation scenarios. The rotation tray is capable of maintaining rotation frequencies of $f = 0.008$ Hz (in the following denoted as the "nonrotating case"), $f = 0.8$ Hz (medium rotation case) and $f = 1.6$ Hz (high rotation case).

A separate set of experimental points were also conducted without a temperature difference ($\Delta T = 0$ K) across the gap. In these cases $\mathrm{R_T} \approx 8.4 \times 10^7$ [cf. Eq. (14)] for both reference temperatures. The Rayleigh-Roberts number which parametrizes internal heating ranges between $8.46 \times 10^5 < \mathrm{R_H} < 1.10 \times 10^7$.

In the case of $\Delta T > 0$, the Rayleigh number $\mathrm{Ra_E}$ [cf. Eq. (22)] ranges between 1.155×10^3 and 4.471×10^5. The

convective parameter $\mathrm{Ra_T}$ ranges between 1.427×10^2 and 4.962×10^4. We find 21 experimental points where convection is dominated by the temperature difference across the gap ($\mathrm{Ra_E}/(2\mathrm{Ra_T}) < 1$) and 139 experimental points where internal heating is dominant ($\mathrm{Ra_E}/(2\mathrm{Ra_T}) > 1$).

In the following, theoretical values of the onset of convection are compared with experimental data. Interferograms of the GeoFlow experiment are used, which are able to highlight even small deviations in the refractive index and hence in the temperature field. A Wollaston shearing interferometry unit is used to visualize flows. The field of view covers about 90 degrees from the north pole to the equator, cf. Fig. 17 (yellow line and camera icon). Here, we refer to Ref. [23] for a detailed description of the interferometry unit of GeoFlow. The interferograms show a base fringe pattern, cf. Figs. 18(a) and 18(d) in the conductive case. Deviations in terms of distorted lines (highlighted in yellow) indicate convection. Two prevailing structures can be observed: (a) a butterfly pattern as result of steep convective downdrafts and (b) narrow parallel structures from sheetlike up- or downwelling. However, arbitrary combinations of both are omnipresent, especially for high Rayleigh numbers.
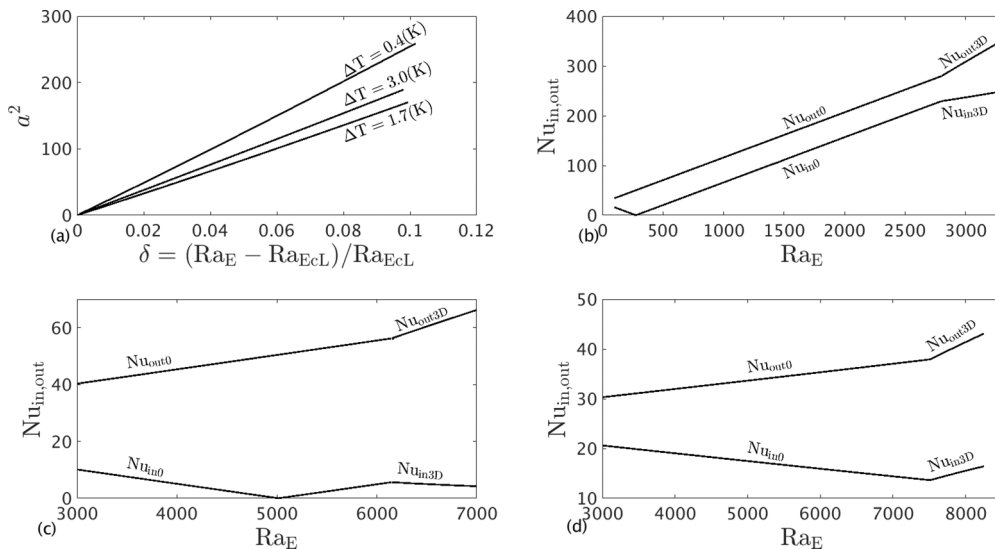

FIG. 16. (a) The amplitude of the supercritical flow and the Nusselt numbers for (b) $\Delta T = 0.4$K, (c) $\Delta T = 1.7$K, and (d) $\Delta T = 3$K for $\eta = 0.5$, Ta $= 17\,200$.

TABLE IV. Constants for the Nusselt numbers from Eq. (58).

$\Delta T (K)$	a_{in3D}	b_{in3D}	a_{out3D}	b_{out3D}
0.4	0.03905	119.80	0.1427	-119.80
1.7	-0.001760	16.46	0.01181	-16.41
3.0	0.003785	-14.77	0.007052	-15.06

Figure 18 shows interferograms of the nonrotating case with $\Delta T = 0$ K, $\Delta T = 0.4$ K and increasing voltages. The corresponding Rayleigh-Roberts numbers in the first case are $R_H = 8.4 \times 10^5$ for $V_{\mathrm{rms}} = 1272$ V, $R_H = 2.3 \times 10^6$ for $V_{\mathrm{rms}} = 2121$ V and $R_H = 4.6 \times 10^6$ for $V_{\mathrm{rms}} = 2969$ V. The critical value of $R_{\mathrm{HcL}} = 1.6 \times 10^6$ takes place between Figs. 18(a) and 18(b), occurring at $V_{\mathrm{rms,crit.}} = 1754$ V. Figure 18(b) shows a clear distortion from the base pattern, which changes to a convective plume for higher voltages, cf Fig. 18(c). Accompanying numerical simulations [22] confirm the existence of convective cells for $V_{\mathrm{rms}} = 2121$ V.

In the case of $\Delta T = 0.4$ K the onset is predicted at $\mathrm{Ra}_{\mathrm{EcL}} = 1511$, which corresponds to $V_{\mathrm{rms,crit.}} = 1456$ V. The transition from the conductive state to the convective regime is depicted in Figs. 18(d) and 18(e), which capture the onset by experimental points with $\mathrm{Ra}_E = 1155$ and $\mathrm{Ra}_E = 3208$, respectively. As in the case of pure internal heating, a convective plume is found for higher voltages. The onset of convection in the case of $\Delta T = 3$ K at $V_{\mathrm{rms,crit}} = 671$ V cannot be verified as the lowest voltage available in the experiment is $V_{\mathrm{rms}} = 1272$ V.

The theoretical onset of convection in the two rotating cases is validated experimentally using the interferograms presented in Fig. 19 for $\Delta T = 0.4$ K, $\Delta T = 1.7$ K, and $\Delta T = 3$ K.

FIG. 18. Experimental interferograms for the nonrotating case for $\Delta T = 0$ K (left-hand column) and $\Delta T = 0.4$ K (right-hand column). The onset of convection is found between (a, b) and (d, e), respectively. While conductive cases show only a base fringe pattern (a, b) the convectively unstable flows appear as butterfly patterns (c, f) for $V_{\mathrm{rms}} = 2969$ V and as distorted fringe lines (b, e) for $V_{\mathrm{rms}} = 2121$ V. Structures are highlighted in yellow to emphasize the thermal structure.
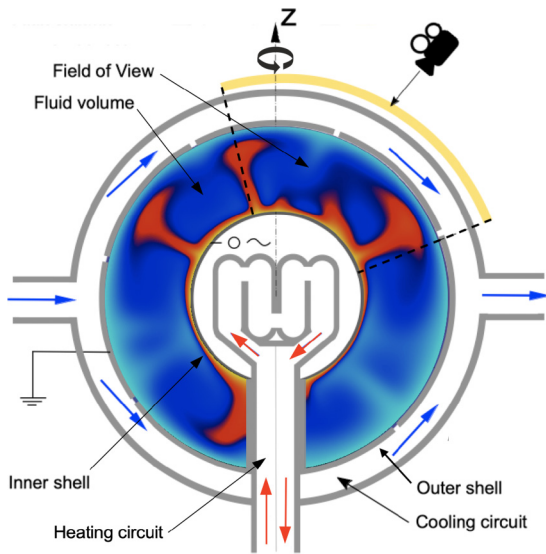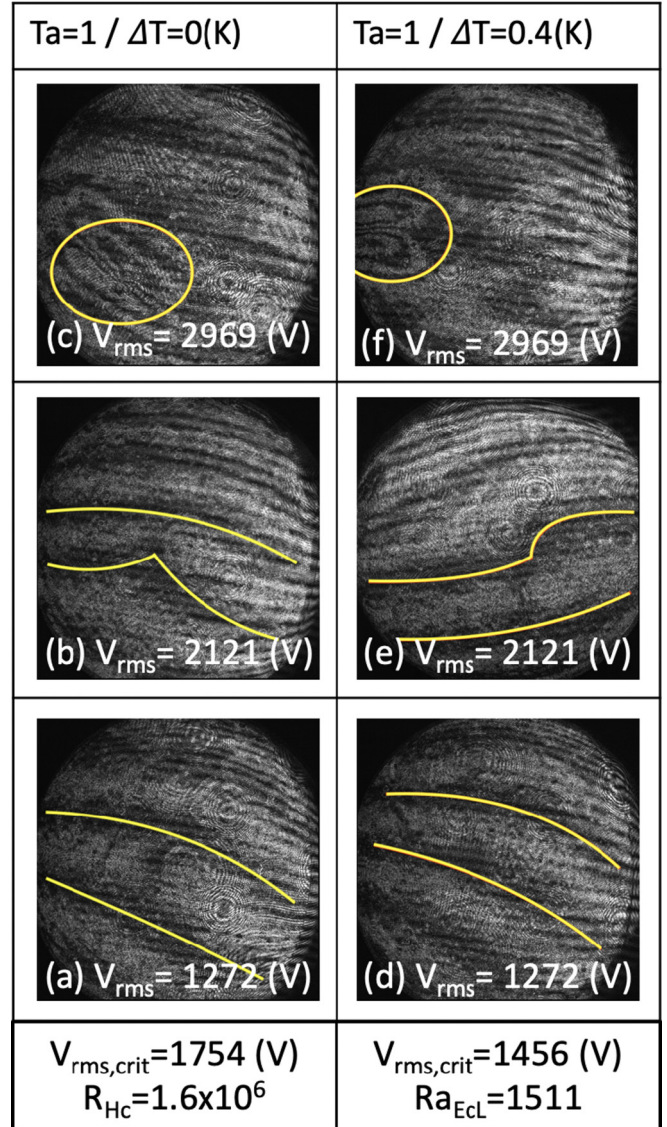

FIG. 17. Sketch of the GeoFlow experiment. The working fluid is thermalized through an inner and outer heating/cooling loop. Interferometry is used to visualize fluid flows (yellow field of view). High voltage is applied to enforce a dielectrophoretic force field, which mimics a radial gravity field. The fluid cell is visualized with a numerical simulation.

Figure 19 depicts 12 cases, showing 11 interferograms. For the case $f = 0.8$ Hz, $\Delta T = 3$ K, no conductive experimental point is present. Here, the onset voltage is below the minimum voltage. Over the entire parameter range, the onset of convection is located within the predicted limits. However, the coarse grid of experimental points of GeoFlow makes it difficult to make more accurate statements about the convective onset. This is based on voltage increments of 921 V and temperature increments of 1.3 K. Hence, the onset cannot be captured more precisely with this setup, but with a mean deviation of 177 V. This is based on the investigation of the 42 interferograms used for this study.
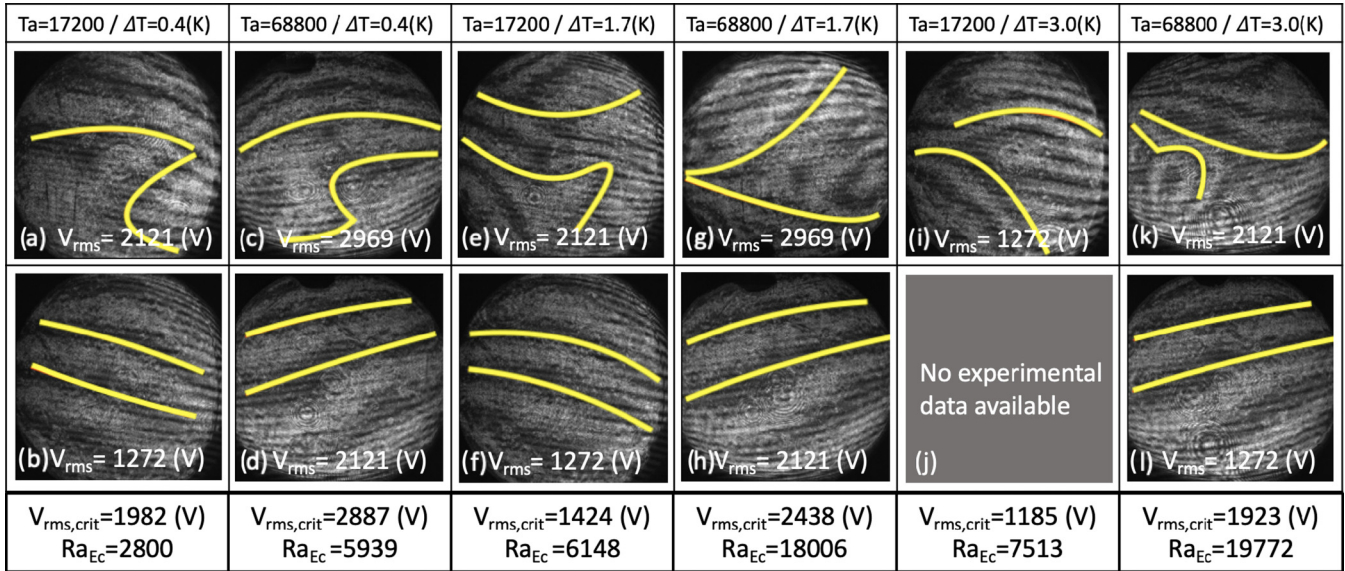
FIG. 19. Experimental interferograms for the rotating case for $\Delta T = 0.4$ K, $\Delta T = 1.7$ K, $\Delta T = 3$ K, $f = 0.8$ Hz (Ta = 17 200), and $f = 1.6$ Hz (Ta = 68 800); see Table II. The upper row depicts convectively unstable flows, the lower row depicts conductive cases. The onset of convection is located in between the two rows.

VII. SUMMARY AND CONCLUSIONS

Our purpose in this paper has been to investigate the influence of dielectrical heating on a convective flow under a radial force field in a nonrotating and rotating spherical gap numerically.

First, we consider the base state in the nonrotating spherical gap with $\Delta T = T_{in} - T_{out} \geqslant 0$. As in the Rayleigh-Bénard convection the basic flow is $\mathbf{U}_0 = 0$ and the temperature is radially dependent. The heat transfer analysis has been performed in terms of the Nusselt number. Whereas in the case of the purely dielectrical heating, i.e., $\Delta T = 0$, the Nusselt numbers or the energy fluxes that leave the domain under consideration through the surfaces are same, the situation is more difficult if the inner surface is warmer than the outer one $\Delta T > 0$. The energy flux that comes from the warmer surface due to the conduction and the energy flux, produced due to the source, have opposite directions that influences the heat transfer.

If the spherical gap rotates (we consider $\Delta T > 0$ only), then the influence of the centrifugal force leads to the formation of a steady, axisymmetric and equatorially symmetrical basic flow that must be calculated numerically. Linear stability theory is used to derive the critical Rayleigh-Roberts number ($\Delta T = 0$ K) and critical Rayleigh number ($\Delta T > 0$) at which the transition from the basic flow into the three-dimensional flow occurs. The first instability does not depend on the Prandtl number in the nonrotating case, as it does in RB convection, because the basic flow becomes unstable with respect to the steady perturbations. In the rotating case, the instability sets in as Hopf bifurcation. Moreover, the basic flow, loses its stability with respect to the three-dimensional perturbations with positive azimuthal wave numbers $m_c > 0$.

Calculating the three-dimensional flows reveals the different behavior of the amplitude. Whereas the bifurcation is subcritical in the nonrotating case, the supercritical one is responsible for the transition if the system rotates.

The numerical results have been compared with outcomes of the GeoFlow experiment. The critical Rayleigh numbers, more precisely the critical voltages, coincide well with observational data within 177 V. Interferograms are analyzed for convection, which are highlighted as distortions in base fringe patterns.

Both numerical and experimental results show that the internal heating plays a crucial role and must be taken into account if the dielectrical fluid is subjected into the fast oscillated electric field. Further numerical investigations should clarify how the high Taylor numbers Ta $= 10^5 \div 10^7$ influence the flow structure and the heat transfer. This issue has relevance for the geophysical applications.

[1] G. Geiger and F. Busse, Geophys. Astrophys. Fluid Dyn. **18**, 147 (1981).

[2] J. W. M. Ardes and F.H. Busse, Phys. Earth. Planet. Inter. **99**, 55 (1993).

[3] F. Busse, J.Fluid Mech. **72**, 67 (1975).

[4] W. Hirsching and F. Busse, Geophys. Astrophys. Fluid Dyn. **72**, 145 (1993).

[5] D. Bercovici, G. Schubert, and G. Glatzmaier, Geophys. Astrophys. Fluid Dyn. **61**, 149 (1991).

[6] F. Feudel, K. Bergemann, L. S. Tuckerman, C. Egbers, B. Futterer, M. Gellert, and R. Hollerbach, Phys. Rev. E **83**, 046304 (2011).

[7] C. Egbers, W. Beyer, A. Bonhage, R. Hollerbach, and P. Beltrame, Adv. Space Res. **32**, 171 (2003).

[8] L. Landau and E. M. Lifshitz, *Electrodynamics of Continuos Media, Landau Lifshitz Course of Theoretical Physics, Vol. 8, 2nd ed.* (Elsevier Butterworth-Heinemann, Burlington, MA, 1984).

[9] R. J. Turnbull and J. R. Melcher, Phys Fluids **12**, 1160 (1969).

[10] J. Melcher, *Continuum Electromechanics* (MIT Press, Cambridge, MA, 1981).

[11] I. Yavorskaya, N. Fomina, and Y. Belyaev, Acta Astronautica **11**, 179 (1984).

[12] B. Futterer, C. Egbers, N. Dahley, S. Koch, and L. Jehring, Acta Astronautica **66**, 193 (2010).

[13] B. Futterer, N. Dahley, S. Koch, N. Scurtu, and C. Egbers, Acta Astronautica **71**, 11 (2012).

[14] B. Futterer, A. Krebs, A.-C. Plesa, F. Zaussinger, R. Hollerbach, D. Breuer, and C. Egbers, J. Fluid Mech. **735**, 647 (2013).

[15] V. Travnikov, C. Egbers, and R. Hollerbach, Adv. Space Res. **32**, 181 (2003).

[16] B. L. Smorodin, Tech. Phys. Lett. **27**, 1062 (2001).

[17] B. L. Smorodin and V. G. Velarde, J. Electrostat. **50**, 205 (2001).

[18] R. Hollerbach, Int. J. Numer. Meth. Fluids **732**, 773 (2000).

[19] P. Roberts, Q. J. Mech. Appl. Math **22**, 211 (1969).

[20] H. Yoshikawa, O. Crumeyrolle, and I. Mutabazi, Phys Fluids **25**, 024106 (2013).

[21] V. Travnikov, O. Crumeyrolle, and I. Mutabazi, Phys Fluids **27**, 054103 (2015).

[22] F. Zaussinger, P. Haun, M. Neben, T. Seelig, V. Travnikov, C. Egbers, H. Yoshikawa, and I. Mutabazi, Phys. Rev. Fluids **3**, 093501 (2018).

[23] F. Zaussinger, A. Krebs, V. Travnikov, and C. Egbers, Adv. Space Res. **60**, 1327 (2017).